Research Square

Preprints are preliminary reports that have not undergone peer review.
They should not be considered conclusive, used to inform clinical practice,
or referenced by the media as validated information.

Poly (aniline-2-sulfonic acid) core-shell gold nanoparticles decorated as a non-enzymatic electrochemical sensor for Dopamine determination

Mohammad Nikfarjam
Shahid Beheshti University
Javad Shabani Shayeh
J_shabani@sbu.ac.ir

Shahid Beheshti University
Roya Sedghi
Shahid Beheshti University

Article

Keywords: Polyaniline, core-shell, Au nanoparticle, electrochemical sensor, Dopamine.

Posted Date: November 25th, 2026

DOI: https://doi.org/10.21203/rs.3.rs-11540593/v1

License: This work is licensed under a Creative Commons Attribution 4.0 International License.
Read Full License

Additional Declarations: No competing interests reported.

Poly (aniline-2-sulfonic acid) core-shell gold nanoparticles decorated as a non-enzymatic electrochemical sensor for Dopamine determination

Mohammad Nikfarjam [a], Javad Shabani Shayeh* [b, c], Roya Sedghi* [a]

[a] *Department of Polymer & Materials Chemistry, Faculty of Chemistry & Petroleum Sciences, Shahid Beheshti University, G.C, 1983969411, Tehran, Iran*

[b] *Protein Research Center, Shahid Beheshti University, G. C., Velenjak, Tehran, Iran*

[c] *Faculty of Life Sciences and Biotechnology, Shahid Beheshti University, Tehran, 1983969411, Iran*

*Corresponding authors.

E-mail Address: r_sedghi@sbu.ac.ir

E-mail address: j_shabani@sbu.ac.ir

Abstract

A novel non-enzymatic electrochemical sensing platform was developed for the sensitive and selective determination of dopamine (DA) based on a magnetic Fe_3O_4@ZnO core–shell nanocomposite functionalized with poly(aniline-2-sulfonic acid) and decorated with gold nanoparticles (Fe_3O_4-ZnO–PA2S–Au). The structural, morphological, and optical characteristics of the synthesized nanocomposite were systematically confirmed by FT-IR, XRD, SEM, TEM, EDX mapping, and DRS. The synergy between the semiconducting magnetic core–shell framework, the π\piπ-conjugated conducting polymer backbone, and the catalytic Au relays significantly facilitated electron-transfer kinetics and enlarged the electroactive surface area. Under optimized square wave voltammetry (SWV) conditions, the modified carbon paste electrode exhibited a wide linear dynamic range of 5.0 to 64.0 μM, a high sensitivity of 50.29 $\mu A \cdot \mu M^{-1}$ (R^2=0.998) with a limit of detection **(**LOD**)** of 0.19 μM and a limit of quantification **(**LOQ**)** of 0.64 μM (S/N=3). Furthermore, differential pulse voltammetry (SWV) demonstrated clear peak separation and robust discrimination against common physiological interferents (Glucose, urea and metal ions). The proposed sensor provides a promising, cost-effective, and highly reproducible analytical tool for clinical diagnostics and neurological monitoring.

Keywords:

Polyaniline, core-shell, Au nanoparticle, electrochemical sensor, Dopamine.

Introduction

Parkinson's syndrome, a multifaceted and globally occurring neurological anomaly, primarily influences the motor system, leading to persistent dysfunctions in the central nervous system [1, 2]. Scientific studies suggest that reduced levels of Dopamine (DA), a key catecholamine present in the central nervous system with a pivotal role in modulating our emotions and cognition, contribute to neurodegenerative and neuropsychiatric disorders[3]. Therefore, the evolution of a sensitive and swift method for detecting DA is crucial for diagnostic and pathological studies.

However, in human blood serum and other specimens, various substances usually interfere with DA (predominantly Vitamin C and Uric Acid) and can disrupt its detection [4, 5].

The clinical quantification of dopamine (DA) relies heavily on electrochemical techniques due to their high sensitivity, rapid response, and operational simplicity [6, 7]. While conventional enzymatic biosensors (e.g., tyrosinase- or laccase-based systems) offer inherent biological specificity, their practical translation remains strictly constrained by poor thermal/chemical stability, complex immobilization protocols, high production costs, and irreversible enzymatic denaturation [8-10]. Consequently, research has decisively transitioned toward non-enzymatic electrochemical sensing platforms based on nanostructured functional materials that used for various analyte detection [11-13]. However, the critical bottleneck in non-enzymatic DA monitoring lies in overcoming severe bio-interference from coexisting electroactive physiological species—principally ascorbic acid (AA) and uric acid (UA). Because AA and UA oxidize at potentials nearly identical to those of DA on bare electrodes and typically exist at concentrations orders of magnitude higher in biological fluids, precise electrode surface engineering is essential. Tailoring nanocomposite architectures with catalytic active sites, tuned surface charges, and accelerated electron-transfer kinetics is therefore imperative to achieve distinct potential separation and robust selectivity without relying on fragile biological recognition elements [11].
In this type of sensor, the electrocatalytic activity of electrode materials is a key factor that affects the sensitivity and selectivity for DA detection [14, 15]. In this regard, noble metal nanoparticles, due to their extraordinary catalytic activities for the oxidation of biological molecules, have been widely used [16].
Considering the unique properties of Au nanoparticles (Au NPs), such as good conductivity, beneficial electrocatalytic capability, and biocompatibility, researchers have dedicated themselves to the construction of DA electrochemical sensors with Au NPs [17]. For this purpose, the control and dispersion of Au NPs size are important factors that can affect the sensitivity of DA detection [18].
Recent advances in electrocatalytic design have introduced a variety of strategies for immobilizing Au NPs onto solid supports, enabling improved catalytic performance [19]. Au NPs integrated with conducting polymers, carbon nanotubes, graphene, and ordered mesoporous carbon have emerged as highly efficient platforms for the direct electrooxidation of DA [20]. Among these

materials, poly(aniline-2-sulfonic acid) (PA2S) stands out as a robust conductive polymer for electrode modification in sensor fabrication. Its sulfonic acid functional groups not only enhance interfacial conductivity but also provide well-defined anchoring sites that promote uniform dispersion and size control of Au NPs, thereby improving electrocatalytic activity.

In this work, we synthesized a nanocomposite (NC) with a semiconducting core made of Iron Oxide and a shell made up of zinc oxide. Then, this core/shell was covered by a Polymerized meta sulfonated Aniline which is decorated with gold NPs. A modified sensing interface using Fe_3O_4, ZnO, PA2S conductor, and Au NPs (Fe_3O_4-ZnO-PA2S-Au NPs) has been synthesized.

A modified carbon paste electrode (CPE) was prepared by thoroughly blending 5 wt% of the synthesized NPs with 95 wt% graphite powder. The resulting mixture was homogenized by adding two to three droplets of paraffin oil using a micropipette until a uniform, malleable paste was obtained. The modified carbon paste was then packed into the electrode cavity, and its surface was smoothed on weighing paper to ensure a reproducible electroactive interface.

Unlike conventional glassy carbon electrodes, carbon paste electrodes (CPEs) offer superior mechanical and renewable surfaces, lower background currents, and straightforward bulk modification. This architecture stably integrates the nanocomposite directly within the carbon matrix as an intrinsic sensing platform, ensuring consistent active-site distribution and enhanced reproducibility.

The proposed sensor significantly advances past electrochemical platforms by drastically minimizing the requisite Au content through the integration of an earth-abundant, synergistic Fe_3O_4-ZnO-PA2S ternary nanocomposite. This architecture establishes a robust Fe_3O_4-ZnO heterojunction coupled to a conductive poly(aniline-co-anthranilic acid) (PA2S) matrix, which promotes rapid intermolecular charge-transfer pathways and reduces charge-transfer resistance while relying on only trace gold loadings. Consequently, the design outperforms existing binary Fe_3O_4-ZnO and conventional Au-rich sensors, delivering a substantially wider linear dynamic range, lower detection limit (LOD), enhanced anti-fouling stability, and superior electrocatalytic selectivity at a markedly lower fabrication cost.

Experimental

Materials and Apparatus

All chemicals were of analytical grade and used as received without further purification. Reagents for nanocomposite synthesis, including ferrous chloride tetrahydrate ($FeCl_2.\ 4H_2O$), ferric chloride hexahydrate ($FeCl_3.\ 6H_2O$), zinc acetate dihydrate ($Zn(CH_3COO)_2.6\ H_2O$), chloroauric acid tetrahydrate ($HAuCl_4.\ 4H_2O$), aniline-2-sulfonic acid (A2S) monomer, ammonium persulfate (APS), diethanolamine, hydrochloric acid (HCl), ammonia solution, ethanol, and methanol, were obtained from Merck and Sigma-Aldrich. Materials for electrode modification and electrochemical measurements, including high-purity graphite powder, binding oil, acetone, potassium ferricyanide($K_3[Fe(CN)_6]$), and phosphate buffer salts (Na_2HPO_4, NaH_2PO_4), were purchased from Merck. Analyte stock solutions were prepared using dopamine hydrochloride (DA), L-ascorbic acid (AA), uric acid (UA), and acetaminophen (APAP), all purchased from Sigma-Aldrich. All solutions were prepared using deionized water. The Fourier transform infrared (FT-IR) spectroscopy over the scanning range of 4000–400 cm^{-1} was acquired with a BOMEM/MB-Series FT-IR spectrophotometer (ABB Bomem Inc., Canada) in the form of KBr pellets with a 2 cm^{-1} resolution. The X-ray diffraction spectroscopy over the scanning angle of 10º-80º was acquired using the XD-3A X-ray diffraction machine, along with Cu Kα radiation. Diffuse reflectance spectroscopy of NCs was investigated by Diffuse reflectance spectroscopy (DRS) S_4100 SCINCO (South Korea). Electrochemical experiments were carried out by potentiostat /Galvanostat (IVIUM-Vertex One- France). A three electrode system include a Pt, Ag/AgCl as counter and references electrode, respectively were used for all electrochemical experiments. We prepare the working electrode as our previous report [21]. Firstly, Fe_3O_4-ZnO-PA2S-Au mixed by graphite powder (5:95 wt%) and after that mineral oil was added to the mixture to form a mortar like shape. Finally, the result paste inserted to as glass tube to carry out the electrochemical experiments. The Artificial cerebrospinal fluid solution was composed by NaCl (125mM), KCl (1mM), KH_2PO_4 (1.2 mM), $NaHCO_3$ (26 mM), $CaCl_2$ (2.5 mM), Glucose (60 μM) and urea 50 μM. The independent analysis were carry out for 3 times.

Synthesis of Iron (II, III) oxide NPs

Ferrous chloride tetrahydrate (0.03 mol) and ferric chloride hexahydrate (0.06 mol) were dissolved in 300 mL of deionized water in a three-necked flask. The resulting solution was maintained at 65

°C under a nitrogen atmosphere with continuous stirring. Subsequently, ammonia solution was introduced dropwise until the pH reached 11.0. The reaction was allowed to proceed for an additional 60 minutes before the suspension was cooled naturally to room temperature. The resulting black Fe_3O_4 nanoparticles were separated, thoroughly rinsed with deionized water until a neutral pH was achieved, and finally dried under vacuum at 60 °C overnight.[22].

Synthesis of Iron (II, III) oxide-Zinc Oxide NCs

The Fe_3O_4/ZnO nanocomposite was synthesized by depositing ZnO onto the surface of Fe_3O_4 nanoparticles via a thermal decomposition process. Initially, 0.49 g of Fe_3O_4 nanoparticles and 3.93 g of zinc acetate dihydrate [$Zn(CH_3COO)_2 \cdot 4H_2O$] were dispersed in 50 mL of ethanol under continuous stirring at 70 °C for 1 h. Subsequently, a solution containing 1.58 mL of diethanolamine and 5 mL of ethanol was added gradually to the reaction mixture. Stirring was maintained until the suspension developed a dark-brown coloration. The reaction was then continued for another 2 h, during which the mixture gradually transformed into a gel. The resulting Fe_3O_4/ZnO nanocomposite was recovered through magnetic decantation, washed successively with 40 mL of deionized water and 40 mL of methanol, and dried under vacuum at 90 °C for 24 h.[23].

Preparation of Fe_3O_4-ZnO-PA2S NCs

The polymer-based nanocomposite was prepared through in situ oxidative polymerization of the PA2S monomer in the presence of Fe_3O_4/ZnO nanoparticles. Initially, 0.80 g of Fe_3O_4/ZnO nanoparticles and 0.21 g of PA2S monomer were dispersed in 60 mL of distilled water. The suspension was subjected to ultrasonic treatment for 10 min to improve the dispersion of the solid components, followed by magnetic stirring for 30 min. Subsequently, 10 mL of 1 M hydrochloric acid was introduced into the suspension, and stirring was maintained for an additional 30 min. An aqueous solution containing 0.51 g of ammonium persulfate was then added dropwise over a period of 10 h to initiate oxidative polymerization. The reaction mixture was continuously stirred for a further period, with the total reaction time reaching 48 h. Upon completion of polymerization, the resulting solid product was separated by filtration and washed three times with distilled water, followed by three washing cycles with absolute ethanol. Finally, the collected nanocomposite was dried in an oven at 90 °C for 7 h.

Preparation of Fe_3O_4-ZnO-PA2S-Au NCs

The Fe_3O_4–ZnO–PA2S–Au nanocomposite was prepared through an aqueous-phase reduction process involving $HAuCl_4$ under thermal conditions. Initially, 0.5 g of the previously synthesized Fe_3O_4–ZnO–PA2S nanocomposite was introduced into a solution containing 0.1 g of $HAuCl_4 \cdot 4H_2O$ in a round-bottom flask. The suspension was sonicated for 30 min to promote effective contact between the gold precursor and the nanocomposite surface. During this stage, Au^{3+} ions were adsorbed onto the polymeric matrix through coordination interactions with nitrogen- and sulfur-containing functional groups (=N– and S–), facilitating their subsequent reduction. The resulting suspension was then heated to boiling and maintained under these conditions for 1 h, leading to the formation of spherical gold nanoparticles. The deposited Au nanoparticles were stabilized by the nitrogen- and sulfur-containing sites of the PA2S polymer. Finally, the synthesized material was recovered by filtration, washed thoroughly with distilled water, and dried in a vacuum oven at 60 °C for 24 h to obtain the final nanocomposite powder. The successive preparation stages of the Fe_3O_4–ZnO–PA2S–Au nanocomposite are illustrated in Scheme 1.

[24].

Results & Discussion

The FT-IR spectra of Fe_3O_4 NPs, Fe_3O_4–ZnO NCs, Fe_3O_4–ZnO–PA2S NCs, and Fe_3O_4–ZnO–PA2S–Au NCs are presented in Figure 1a. The spectrum of Fe_3O_4 exhibits two characteristic bands: a broad absorption at 3000–3500 cm^{-1}, attributed to surface –OH groups of iron (II, III) oxide, and a band near 550 cm^{-1} corresponding to Fe–O bending vibrations [22]. Upon coating Fe_3O_4 with a ZnO shell, noticeable changes appear in the metal-oxide region, confirming successful shell formation. Specifically, the intensity in the 3000–3500 cm^{-1} region increases, and the metal–oxygen band broadens to 450–560 cm^{-1}, consistent with Zn–O/Fe–O interactions [23]. The introduction of PA2S onto the Fe_3O_4–ZnO surface is evidenced by absorptions in the 3000–3500 cm^{-1} region associated with the N–H_2 stretching vibrations of aniline. Additional distinct bands at 1080, 750, and 620 cm^{-1} correspond to S=O, S–O, and C–S vibrations, respectively,

confirming the presence of sulfonic functional groups and successful polymer grafting. Furthermore, polymerization of sulfonated aniline on the NC surface generates intense absorptions in the 1500–1800 cm^{-1} region, arising from the abundant organic moieties (AOM) within the PA2S layer (Figure 1a).

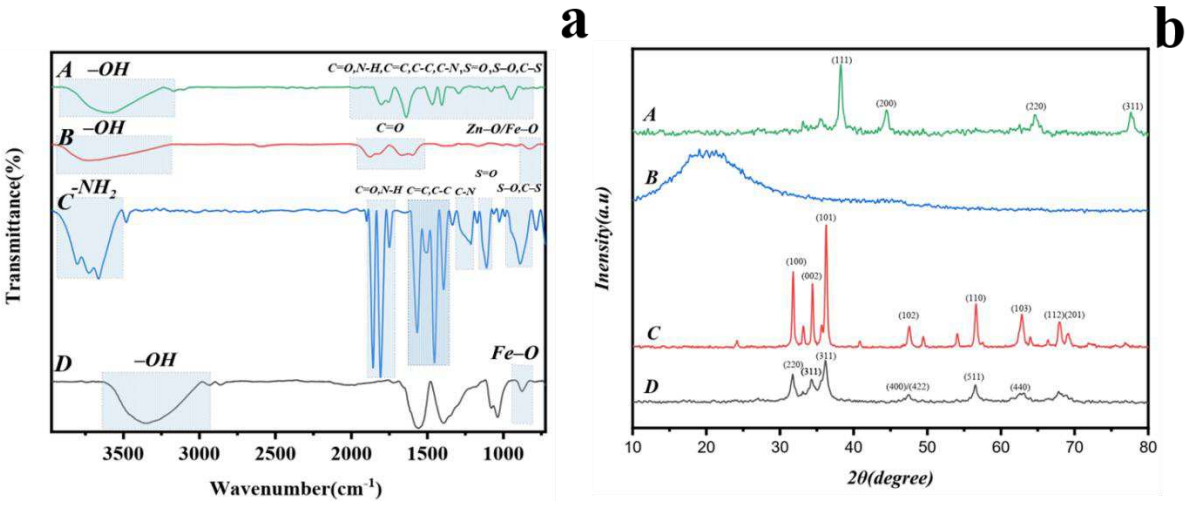

Figure 1. a, FT-IR spectra of (A) Fe_3O_4-ZnO-PA2S-Au NC, (B)Fe_3O_4-ZnO NC, (C)Fe_3O_4-ZnO-PA2S NC & (D) Fe_3O_4 NP. b, X*RD Patterns of* (A) Fe_3O_4-ZnO-PA2S-Au NC, (B) Fe_3O_4-ZnO-PA2S NC, (C) Fe_3O_4-ZnO NC & (D) Fe_3O_4 NP

The XRD pattern of Fe_3O_4 nanoparticles displays characteristic reflections at 2θ = 31°, 34°, 36°, 47°, 56°, and 62°, which correspond to the (220), (311), (311/101), (400/422), (511), and (440) planes of the spinel Fe_3O_4 structure, confirming the formation of magnetite nanoparticles. Upon coating Fe_3O_4 with a ZnO shell, eight additional peaks emerge at 31.84°, 34.52°, 36.33°, 47.63°, 56.71°, 62.96°, 68.13°, and 69.18°, which match the (100), (002), (101), (102), (110), (103), (112), and (201) planes of hexagonal wurtzite ZnO. These reflections verify the successful deposition of a ZnO layer around the Fe_3O_4 core. During polymer functionalization, partial broadening and merging of the metal oxide peaks indicate the formation of an amorphous PA2S layer surrounding

the Fe_3O_4–ZnO core–shell structure. Finally, the XRD pattern of the fully assembled nanocomposite exhibits distinct peaks at 38°, 45°, 65°, and 78°, corresponding to the (111), (200), (220), and (311) planes of face-centered cubic (FCC) gold. These reflections confirm the successful attachment of Au nanoparticles onto the polymer-coated Fe_3O_4–ZnO surface (figure1b) [24]. The uniform spherical morphology of Fe_3O_4-ZnO-PA2S-Au is evident from fig 2. SEM images indicate a change in the size distribution range of the NPs, which indicates that the gold nanoparticles are uniformly dispersed on the surface. As shown in TEM images, Dark dots with an average diameter of approximately 10 nm correspond to the gold nanoparticles. At the same time, the two distinct gray contrasts observed within each particle confirm the formation of a core–shell structure Fig. 2.

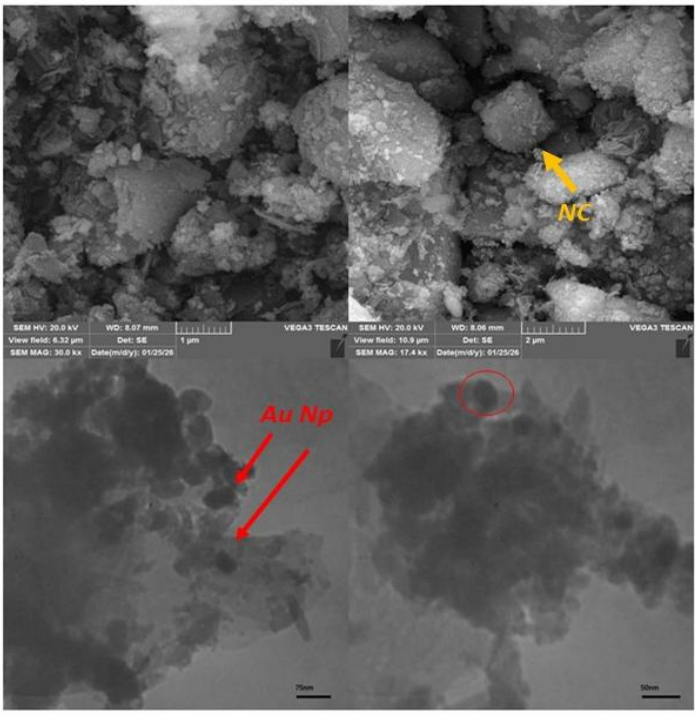

Figure 2. SEM & TEM images of Fe_3O_4-ZnO-PA2S-Au NC

Additionally, the elemental content of Fe_3O_4-ZnO-PA2S-Au NC was evaluated by EDX. As seen in Fig 3a, the synthesized compound primarily consists of Iron and Oxygen - the two main elements forming the Core of the NC. Meanwhile, the zinc peak in EDX analysis indicates formation of a ZnO layer on the iron (II, III) Oxide core. The synthesized compound consists of Carbon and Nitrogen, the two main elements forming the monomer. Additionally, the Sulfur element, resulting from the connection of the Sulfonic Acid group to the monomer, and the Gold metal, resulting

from the deposition and reduction of Gold salt on the Fe_3O_4-ZnO-PA2S, are also observed in the EDX spectrum (Fig. 3a.

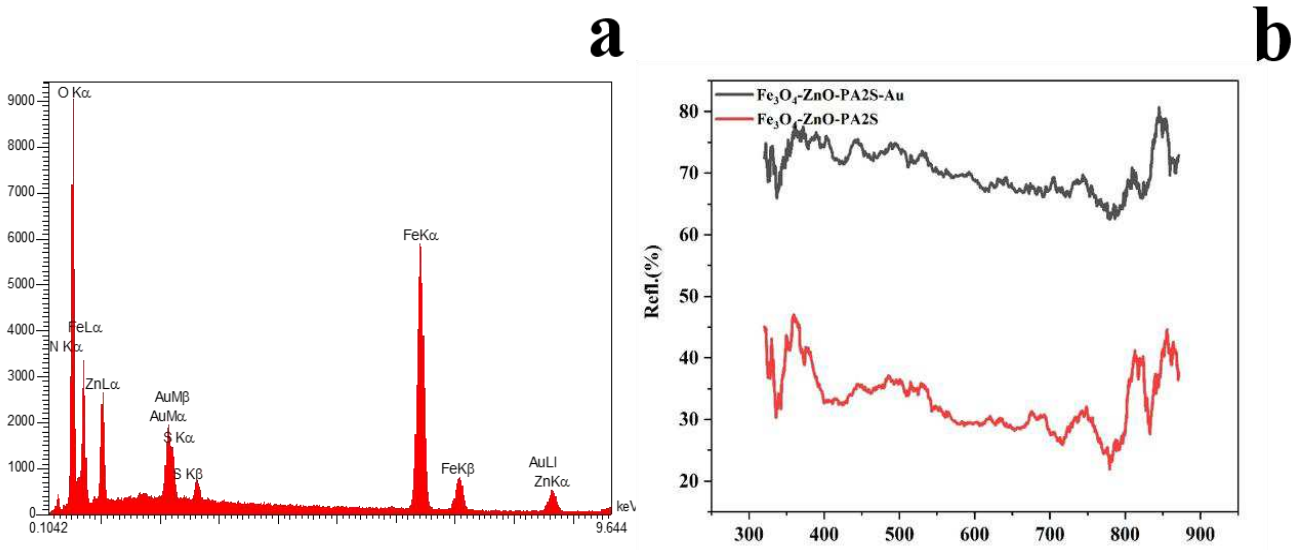

Figure 3. a, EDX Analysis of Fe_3O_4-ZnO-PA2S-Au. b, DRS Analysis of Fe_3O_4-ZnO-PA2S NC & Fe_3O_4-ZnO-PA2S-Au NC

Furthermore, the distribution of elemental content of Fe_3O_4-ZnO-PA2S-Au was evaluated by SEM Mapping. The distribution of Gold NPs, Carbon, Iron, Nitrogen, Oxygen, Sulfur, and Zinc elements can be observed; the distribution of these two (Gold & Sulfur) elements with significantly lower density is noticeable in the final synthesized compound structure fig S1. Additionally, the conductivity of NCs was investigated by DRS of the two polymeric compounds, with and without gold NPs. It indicates a significant increase in emissive photons in the compound containing gold compared to the NC without gold. Examining the DRS spectrum of the two polymer compounds shows a great decrease in the bandgap of the compound after the addition of gold nanoparticles. On the other hand, with the reduction of the bandgap, the intensity of Photon reflection from the NC with gold NPs has increased (40% to 75%), which indicates an increase in conductivity from the gold-free NC compared to the final composition Figure 3b.

Dopamine is a neurotransmitter and hormone that plays a crucial role in various brain functions, including movement, motivation, pleasure, and reward. This Aromatic organic compound has two

hydroxyl and an Amine functional group. These three functional groups have five pairs of nonbonding electrons, which can act as a Lewis base [25]. In the oxidation phase, the analyte would absorb a proton and act as a base, and in the reduction phase, it will lose the proton and act as an acid.

The high electrocatalytic performance of the quaternary composite stems from a coordinated synergy among its constituent phases: trace Au nanoparticles serve as high-turnover catalytic relay centers that lower analyte redox overpotentials and facilitate interfacial electron tunneling, while the Fe_3O_4-ZnO semiconductor heterojunction broadens the electroactive surface area, promotes Fe_3^{2+}/Fe^{3+} multi-valent cycling, and suppresses charge recombination. Concurrently, the functionalized PA2S conductive matrix provides extended π-conjugated pathways that stably anchor the nanostructures and accelerate bulk-to-electrode charge transport. Together, these components establish a cascade electron-transfer highway, yielding significantly amplified redox current responses and superior sensing kinetics with minimal noble-metal consumption.

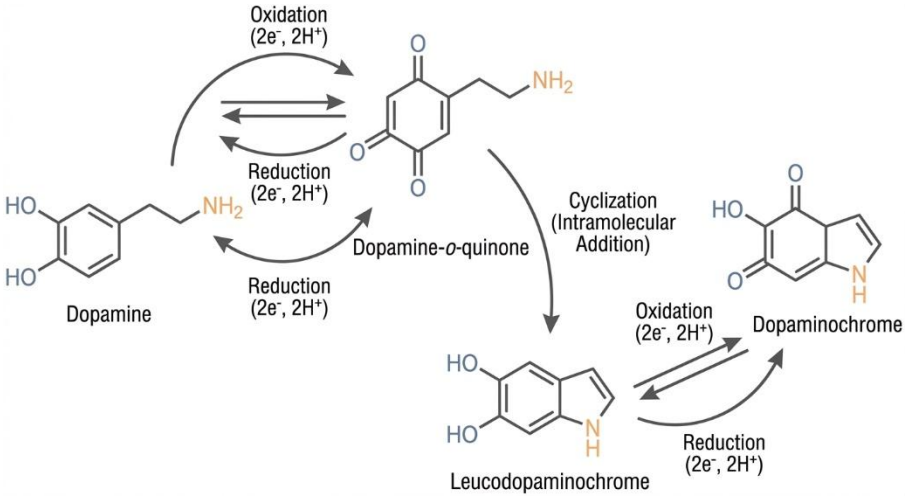

Scheme 1. Oxidation-Reduction Cycle of Dopamine

In order to examine the conductivity of the sensing interface, Cyclic Voltammetry (CV) tests were conducted in $K_3Fe(CN)_6$. The results show significantly higher current in the modified carbon paste electrode (CPE), indicating that the modified electrode with Fe_3O_4-ZnO-PA2S-Au NC has a much higher conductivity than standard CPE electrodes. The surface area of the modified CPE is much higher than that of standard CPE; It shows a higher amount of electrical charge transfer,

which can be attributed to a much higher active surface of Fe_3O_4-ZnO-PA2S-Au NC in comparison to Standard CPE Figure 4A.

In order to examine the detection capabilities of the modified CPE, different analytes were added to the buffer solution. CV results of the modified electrode show that the synthesized NC could detect three different biomolecules: Dopamine, Ascorbic Acid, and Uric Acid. CV schematic of DA has two peaks for oxidation and reduction of this analyte at 0.2 V and 0.09 V, respectively. The AA graph shows only a broad yet single peak of oxidation at 0.35 V. The UA bar graph also has a single peak of oxidation at 0.22 V, but with a much lower Current intensity in the oxidation potential Figure 4B.

Since the broad oxidation peak of AA can cover up the DA peak, we examined the selectivity of our sensor by detecting DA in the presence of AA in the buffer solution through square wave Voltammetry (DPV). The modified electrode effectively resolves the overlapping oxidation signals of DA and AA, shifting the DA peak to a lower potential (0.1 V shift), which eliminates signal interference, a critical requirement for physiological sensing.

It also showed two peaks, the major one at 0.4 V and the second one at 0.65 V, respectively; DA showed a single sharp peak, which was shifted to a lower potential by a value equal to 0.1V (Fig 4C).

The electrochemical behaviour of the system was assessed using square wave voltammetry (SWV). A calibration curve was constructed by correlating the anodic peak current (μA) with analyte concentration (μM) using a standard-addition protocol. The initial solution contained 5 μM analyte in a 50 mL final volume, and successive additions of 10 μL aliquots of a 1 mM standard solution increased the concentration incrementally, producing a working range of approximately 5-64 μM. The SWV peak current increased linearly with concentration, yielding a calibration equation of the form.

The limit of detection (LOD) and limit of quantification (LOQ) were determined using the standard IUPAC definitions:

$$\text{LOD} = \frac{3S}{M} = \frac{3(3.21)}{50.29} = 0.19\ \mu\text{M}$$

$$\text{LOQ}\} = \frac{10S}{M} = \frac{10(3.21)}{50.29} = 0.64\ \mu\text{M}$$

where S = 3.21 is the standard deviation of blank measurements (n = 10) and m = 50.29A/M is the calibration slope from the revised regression equation Ip = 50.29C + 0.514 R^2 = 0.99, completely omitting unstandardized bracket notations.

with a correlation coefficient of R^2 = 0.99 . Based on this calibration, the analytical performance metrics were determined as follows: LOQ = 0.64 µM, and LOD = 0.19 µM. These results confirm reliable linearity and robust electroanalytical performance within the investigated concentration window Figure 4D.

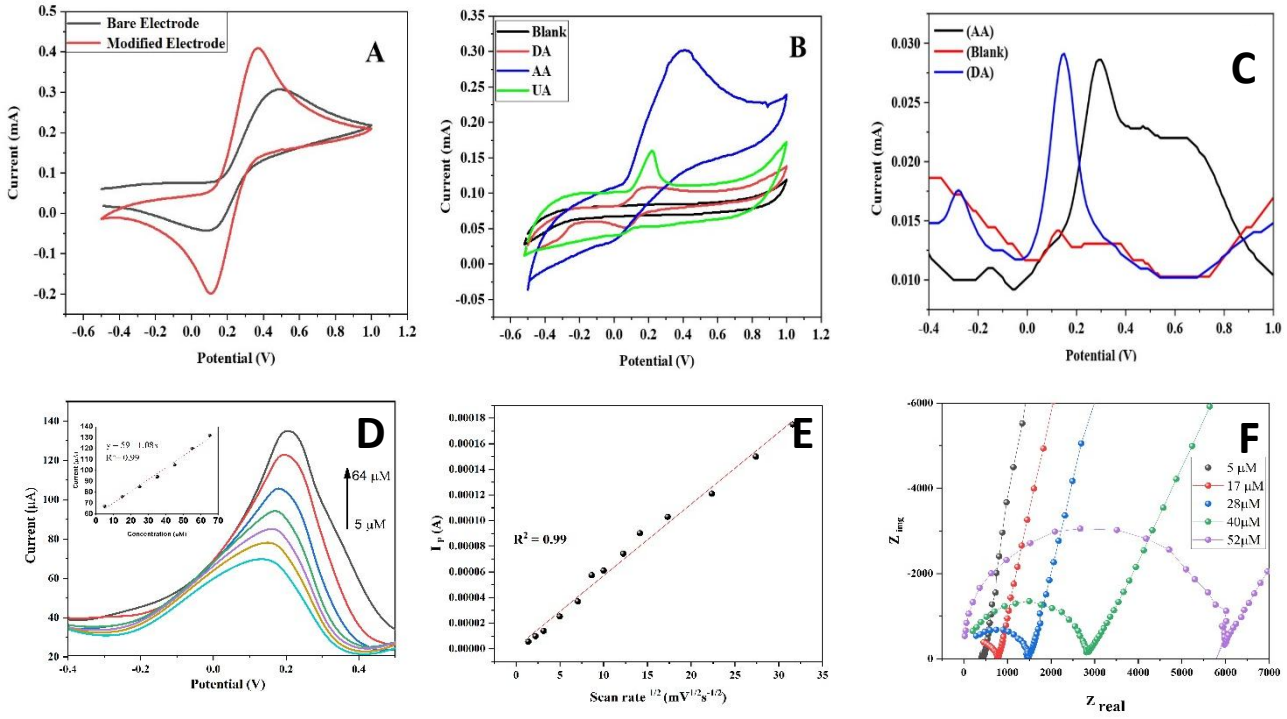

Fig 4. CV curves of CPE bare and modified electrode in K4Fe(CN)6 solution (A), CV curves prepared electrode at the presence of DA, AA and UA (B), DPV results of prepared electrode in the presence of AA and DA (C), DPV curve of prepared electrode at various concentrations of DA (D), I vs root of scan rate for prepared electrode in the presence of DA 5µM (E), Nyquist plot of prepared electrode at various concentrations of DA (F).

To elucidate the mass-transport mechanism of DA at the Fe_3O_4–ZnO–PA_2S–Au NP/CPE, cyclic voltammetric measurements were performed over the scan rate range of 2–1000 mV s^{-1}. The anodic peak current increased linearly with the square root of the scan rate according to Ip (µA) =5.588 $\nu^{1/2}$ +1.092 (R^2 = 0.9905), whereas the correlation with ν itself was markedly weaker (R2=0.889). Moreover, the slope of the log Ip vs log ν plot was determined to be 0.553 (R2=0.9916), which is close to the theoretical value of 0.5 predicted by the Randles–Ševčík equation for an ideal diffusion-controlled process, rather than the value of 1.0 expected for an adsorption-confined process. These results confirm that the electrochemical oxidation of DA at the modified electrode is governed predominantly by diffusion control, consistent with the "cascade electron-transfer highway" provided by the Au catalytic relays and the π-conjugated PA_2S backbone fig 5(F).

Electrochemical impedance spectroscopy was employed to monitor the interfacial properties of the electrode at each stage of modification (Fig. 5(G)). The Nyquist plot of the bare CPE exhibits a semicircle with a charge-transfer resistance (Rct) of ≈ 0.5–0.7 kΩ and a linear Warburg tail (slope ≈ 0.68), characteristic of a diffusion-limited process[13]. Upon sequential immobilization of Fe_3O_4 NPs, ZnO, the PA_2S polymer, and Au nanoparticle decoration, the diameter of the semicircle increases progressively, with the total impedance rising from ≈ 1.4 kΩ (bare CPE) to ≈ 11 kΩ for the fully assembled Fe_3O_4–ZnO–PA_2S–Au NP/CPE. This monotonic growth in Rct confirms the successful stepwise deposition of each component and reflects the semiconducting and polymeric nature of the multilayer film, which imposes an additional barrier to interfacial electron transfer. Nevertheless, the large electroactive surface area and the strong π–π and electrostatic interactions between the PA_2S backbone and dopamine ensure efficient analyte preconcentration at the modified interface, underpinning the sensor's high sensitivity.

Table 1. Comparison of the performance of the prepared sensor with other reports.

Material	Dynamic Range	Limit of detection	Reference
graphene sheets/Congo red	10–190 µM	0.327 µM	[25]
Ni-MOF	0.136~70.0 µM	0.041 µM	[26]
MoS_2/Ni	50–3600 µM	2.1 µM	[27]
Cu-MOF/MWCNT	2 - 180 µM	0.32 µM	[28]
NiO/CuO	0.3–40µM	1.33 µM	[29]
Au/RGO	0.02 - 10 µM	0.02 - 10 µM	[14]
$Ti_3C_2Cl_2$	10 µM − 2000 µM	0.7 µM	[30]
Fe_3O_4-ZnO-PA_2S-Au NP	5-6.5 µM	0.19 µM	This work

Table 1 presents the performance of the prepared electrode compared to some other reports. As can be seen, the Fe3O4-ZnO-PA2S-Au NP electrode The proposed sensor exhibits competitive analytical performance compared to established literature benchmarks, demonstrating high sensitivity and a low limit of detection (LOD). For study the repeatability and reproducibility of prepared electrode, the DA analyte was diluted in Artificial cerebrospinal fluid and detected by DPV. Furthermore, glucose and urea were added to the solution due to analysis of electrode selectivity. The results suggest that the prepared electrode has a competitive performance with other electrodes and can be apply among interferents (Table 2).

Table 2, recovery percents of DA from aCSF

Sample	Determined (μM)	Spiked (μM)	Total found (μM)	Recovery (%)	RSD (%)
aCSF	0	5	5.00 ± 0.04	100.0	2.14
		15	15.08 ± 0.37	100.5	2.58
		25	24.73 ± 0.51	98.92	2.38

These results show that the electrode can be a good candidate for dopamine electrochemical determination.

Conclusion

This work introduces a distinctly engineered Fe_3O_4-ZnO-PA_2S-Au nanocomposite as a novel and highly efficient platform for non-enzymatic dopamine sensing, demonstrating a level of performance that surpasses conventional carbon-based electrodes. Comprehensive structural and electrochemical analyses verified the successful integration of the hybrid components, resulting in markedly enhanced conductivity, accelerated charge-transfer kinetics, and a substantially enlarged electroactive surface area. The sensor's ability to achieve a low detection limit, maintain excellent

linearity, and selectively discriminate dopamine from major physiological interferents highlights its technical superiority and practical robustness. These advancements underscore the novelty of the material design and its capability to address persistent challenges in dopamine detection. Overall, the proposed sensing platform represents a significant step forward toward low-cost, high-performance electrochemical diagnostics.

Acknowledgements

Funding:

The authors received no financial support for the research, authorship and publication of this article.

References

[1] M. Díaz Castela, P. Prendes Fernández, S. Heres Bruck, E. Suárez San Martín, C. García Fernández, J. Sol Álvarez, B. Lozano Aragoneses, A. Sáiz Ayala, E. Santamarta Liébana, J. Álvarez Carriles, L. González Álvarez, M. Blázquez Estrada, Parkinsonism-hyperpyrexia, a rare consequence of deep brain stimulator malfunction in advanced Parkinson's disease, Clinical Parkinsonism & Related Disorders, 10 (2024) 100246.
[2] E. Fiorenzato, S. Moaveninejad, L. Weis, R. Biundo, A. Antonini, C. Porcaro, Brain Dynamics Complexity as a Signature of Cognitive Decline in Parkinson's Disease, Movement Disorders, 39 (2024) 305-317.
[3] T.H.C. Cheung, Y. Ding, X. Zhuang, U.J. Kang, Learning critically drives parkinsonian motor deficits through imbalanced striatal pathway recruitment, Proceedings of the National Academy of Sciences, 120 (2023) e2213093120.
[4] C. Cassel, T. Fulmer, Achieving Diagnostic Excellence for Older Patients, JAMA, 327 (2022) 919-920.
[5] D.J. Handelsman, F. Bacha, M. DeBono, S. Sleiman, M.R. Janu, Sexually transmitted doping: The impact of urine contamination of semen, Drug Testing and Analysis, 14 (2022) 1623-1628.
[6] F. Achi, A.M. Attar, A. Ait Lahcen, Electrochemical nanobiosensors for the detection of cancer biomarkers in real samples: Trends and challenges, TrAC Trends in Analytical Chemistry, 170 (2024) 117423.
[7] J. Han, S. Liu, Z. Wang, Y. Wu, Micro/nanofluidic-electrochemical biosensors for in situ tumor cell analysis, TrAC Trends in Analytical Chemistry, 157 (2022) 116799.
[8] H. Khan, M.R. Shah, J. Barek, M.I. Malik, Cancer biomarkers and their biosensors: A comprehensive review, TrAC Trends in Analytical Chemistry, 158 (2023) 116813.
[9] C. Erkmen, O. Selcuk, D.N. Unal, S. Kurbanoglu, B. Uslu, Layer-by-layer modification strategies for electrochemical detection of biomarkers, Biosensors and Bioelectronics: X, 12 (2022) 100270.
[10] Y. Li, L. Luo, Y. Kong, Y. Li, Q. Wang, M. Wang, Y. Li, A. Davenport, B. Li, Recent advances in molecularly imprinted polymer-based electrochemical sensors, Biosensors and Bioelectronics, 249 (2024) 116018.

[11] J. Li, L. Li, j. Fei, P. Zhao, J. zhao, Y. Xie, Ultrasensitive electrochemical sensor for fenitrothion based on MIL-125 derived iron/titanium bimetallic oxides doped porous carbon composite, Microchemical Journal, 200 (2024) 110426.
[12] Y. Li, M. Zhang, Y. Huang, P. Zhao, J. Zhao, J. Fei, Y. Xie, An ultrasensitive 4-aminophenol electrochemical sensors based on zinc and nitrogen-doped γ-cyclodextrin composites, Microchemical Journal, 197 (2024) 109905.
[13] G. Li, Y. Zhang, R. Zhu, Z. Liu, Y. Jin, N. Ma, X. He, An efficient electrochemical sensor based on ZIF-8 MOF-derived N-containing porous carbon supported Fe3O4 nanoparticles for sensitive detection of ciprofloxacin residues in foods, Microchemical Journal, (2025).
[14] Q. Tian, Y. She, Y. Zhu, D. Dai, M. Shi, W. Chu, T. Cai, H.-S. Tsai, H. Li, N. Jiang, L. Fu, H. Xia, C.-T. Lin, C. Ye, Highly Sensitive and Selective Dopamine Determination in Real Samples Using Au Nanoparticles Decorated Marimo-like Graphene Microbead-Based Electrochemical Sensors, Sensors, 2023, pp. 2870.
[15] E. Vidal, C.E. Domini, D.C. Whitehead, C.D. Garcia, From glow-sticks to sensors: single-electrode electrochemical detection for paper-based devices, Sensors & Diagnostics, 1 (2022) 496-503.
[16] K. Hajra, D. Maity, S. Saha, Recent advancements of metal oxide nanoparticles and their potential applications: A review, Adv. Mater. Lett, 15 (2024) 2401-1740.
[17] K. Lu, J. Liu, X. Dai, L. Zhao, Y. Yang, H. Li, Y. Jiang, Construction of a Au@MoS2 composite nanosheet biosensor for the ultrasensitive detection of a neurotransmitter and understanding of its mechanism based on DFT calculations, RSC Advances, 12 (2022) 798-809.
[18] J.P. Oña, R.-M. Latonen, N. Kumar, M. Peurla, I. Angervo, H. Grénman, Electrocatalytic hydrogenation of glucose and xylose using carbon fiber supported Au nanocatalysts, Electrochimica Acta, 426 (2022) 140754.
[19] R. Mehek, N. Iqbal, T. Noor, Z.A. Ghazi, M. Umair, Metal–organic framework derived vanadium oxide supported nanoporous carbon structure as a bifunctional electrocatalyst for potential application in metal air batteries, RSC Advances, 13 (2023) 652-664.
[20] Z. Cui, Z. Li, Y. Jin, T. Ren, J.a. Chen, X. Wang, K. Zhong, L. Tang, Y. Tang, M. Cao, Novel magnetic fluorescence probe based on carbon quantum dots-doped molecularly imprinted polymer for AHLs signaling molecules sensing in fish juice and milk, Food Chemistry, 328 (2020) 127063.
[21] J. Shabani-Shayeh, A. Ehsani, M. Jafarian, Physioelectrochemical Investigation of Electrocatalytic Activity of Modified Carbon Paste Electrode in Alcohol Oxidation as Anode in Fuel Cell, 전기화학회지, 17 (2014) 179-186.
[22] M. Shashank, H.S.B. Naik, G. Nagaraju, R.S. Keri, M.M. Naik, K. Lingaraju, Facile Synthesis of Fe3O4/ZnO Nanocomposite: Applications to Photocatalytic and Antibacterial Activities, Journal of Electronic Materials, 50 (2021) 3557-3568.
[23] R. Sedghi, Z. Pezeshkian, Fabrication of non-enzymatic glucose sensor based on nanocomposite of MWCNTs-COOH-Poly(2-aminothiophenol)-Au NPs, Sensors and Actuators B: Chemical, 219 (2015) 119-124.
[24] G. Dalla Torre, J.I. Mujika, J.I. Lachowicz, M.J. Ramos, X. Lopez, The interaction of aluminum with catecholamine-based neurotransmitters: can the formation of these species be considered a potential risk factor for neurodegenerative diseases?, Dalton Transactions, 48 (2019) 6003-6018.
[25] Y. Mao, Y. Bao, S. Gan, F. Li, L. Niu, Electrochemical sensor for dopamine based on a novel graphene-molecular imprinted polymers composite recognition element, Biosensors and Bioelectronics, 28 (2011) 291-297.
[26] Q. Xiong, S. Chen, L. Pei, J. Liu, Y. Yang, M. Lu, Y. Song, High-selective dopamine electrochemical sensor based on yolk-shell structural composites derived from Ni-MOF@COFTAPB-DVA, Microchemical Journal, 210 (2025) 112987.

[27] A.U. Rehman, M. Anwar, A. Khan, K.A. Kalhoro, C. Zhang, Y. Zhang, M. Shokouhimehr, Z. Liu, Perforated MoS2 nanosheets adorned with Ni nanoparticles: An electrochemical sensor for concurrent detection of dopamine and uric acid, Microchemical Journal, 209 (2025) 112821.
[28] G. Wang, T. Tang, R. Liu, J. Li, Y. Xu, S. Liao, Novel Electrochemical Sensor Based on Cu-MOF/MWCNT-COOH for the Simultaneous Detection of Ascorbic Acid and Dopamine, Langmuir, 41 (2025) 4102-4112.
[29] B. Liu, X. Ouyang, Y. Ding, L. Luo, D. Xu, Y. Ning, Electrochemical preparation of nickel and copper oxides-decorated graphene composite for simultaneous determination of dopamine, acetaminophen and tryptophan, Talanta, 146 (2016) 114-121.
[30] U. Amara, B. Sarfraz, K. Mahmood, M.T. Mehran, N. Muhammad, A. Hayat, M.H. Nawaz, Fabrication of ionic liquid stabilized MXene interface for electrochemical dopamine detection, Microchimica Acta, 189 (2022) 64.

Supplementary Files

This is a list of supplementary files associated with this preprint. Click to download.

- suplomenterydata.docx